A Characteristic Finite Element Method with Local Mesh Refinements for the Lamm Equation in Analytical Ultracentrifugation

Jiangguo Liu,[1] **Chaoping Chen**[2]
[1] *Department of Mathematics, Colorado State University, Fort Collins, Colorado 80523-1874*

[2] *Department of Biochemistry and Molecular Biology, Colorado State University, Fort Collins, Colorado 80523-1870*

Received 12 November 2007; accepted 25 January 2008
Published online 8 April 2008 in Wiley InterScience (www.interscience.wiley.com).
DOI 10.1002/num.20344

The Lamm equation is a fundamental differential equation in analytical ultracentrifugation, for describing the transport of solutes in an ultracentrifuge cell. In this article, we present a characteristic finite element method with local mesh refinements for solving the Lamm equation. The numerical method is mass-conservative by design and allows relatively large time steps to be used. Numerical experiments indicate that the numerical solutions are oscillation-free in the region near the cell bottom, where mass build up and large concentration gradients occur. Positivity of solutions is also well kept. © 2008 Wiley Periodicals, Inc. Numer Methods Partial Differential Eq 25: 292–310, 2009

Keywords: analytical ultracentrifugation (AUC); characteristic method; convection–diffusion; finite element method; Lamm equation; local mesh refinements

I. INTRODUCTION

Analytical ultracentrifugation (AUC) is a biological analysis that provides first-principle hydrodynamics and thermodynamics information on nearly any biological species, over a wide range of solute concentrations and in a wide range of solvents. It is nondestructive and rapid, and does not require standards for comparison. Therefore, it has been a viable tool for biochemistry and molecular biology. Two complimentary methods are available using an AUC: sedimentation velocity and sedimentation equilibrium. The former provides information about the size and shape of a molecule, whereas the latter provides information about the solution molar mass, association constants, and solution nonideality [1].

The major components of a typical ultracentrifuge are an ultracentrifuge cell, a high speed rotor, and an optical detector. The angular velocity ω of the rotor ranges from $15,000$ rpm (revolutions per minute) to $60,000$ rpm. The strong centrifugal force drives the biological particles

Correspondence to: Jiangguo Liu, Department of Mathematics, Colorado State University, Fort Collins, Colorado 80523-1874 (e-mail: liu@math.colostate.edu)

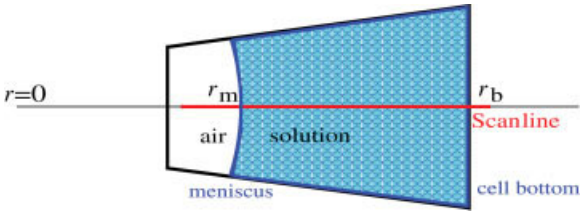

FIG. 1. A cross section in an ultracentrifuge cell (not to scales). [Color figure can be viewed in the online issue, which is available at www.interscience.wiley.com.]

in the ultracentrifuge cell to move toward the cell bottom. The optical detector system scans regularly in the radial direction to record the concentration distribution at different time moments during the centrifugation process, which takes from about 1 h to 2 days. As illustrated in Fig. 1, the ultracentrifuge cell is a tiny container that has the shape of a truncated sector of a cylinder. We use r_m to denote the radial position of the air-liquid meniscus, r_b the radial position of the cell bottom, $r_b - r_m$ the length of the solution column, h the depth of the solution column, and θ the sector angle. Typically, r_m ranges from 5.8 to 6.5 cm, r_b is about 7.2 cm, h ranges from 1.5 to 30 mm, and $\theta = 2°–4°$.

The Lamm equation for the sedimentation of a single species is [2]

$$\frac{\partial c}{\partial t} = \frac{1}{r}\frac{\partial}{\partial r}\left(rD\frac{\partial c}{\partial r} - \omega^2 r^2 sc\right), \qquad r \in [r_m, r_b], \quad t \in [t_0, t_f], \tag{1}$$

where r is the radial position, $c = c(r,t)$ is the unknown concentration distribution, s, D are sedimentation and diffusion coefficients of the solute that might depend on the unknown concentration, and t_0, t_f are the initial and final simulation times. In the derivation of the Lamm equation [2], it is assumed that the solution is incompressible and at mechanical and thermal equilibrium. Accompanying the equation, an initial condition is specified

$$c(r, t_0) = c_0(r), \qquad r \in [r_m, r_b]. \tag{2}$$

In the simplest case, $c_0(r) \equiv$ const, corresponding to an initial uniform loading concentration. It is also clear that the fluid does not go beyond the meniscus or the cell bottom, and so the total flux vanishes at these two ends:

$$\left[rD\frac{\partial c}{\partial r} - \omega^2 r^2 sc\right]_{r=r_m} = 0, \qquad \left[rD\frac{\partial c}{\partial r} - \omega^2 r^2 sc\right]_{r=r_b} = 0. \tag{3}$$

Since its introduction in 1929 [2], the Lamm equation has played a fundamental role in the mathematical modeling of AUC. The early effort on its research was focused on derivations of its analytical or approximate analytical solutions in some limiting cases [2]. This approach is limited, since many of the analytical or approximate analytical solutions are based on idealizations such as an infinite solution column or no diffusion. Instead, numerical methods for the Lamm equation are now the main tool because of their accuracy, efficiency, and flexibility. For example, one can take experimental scans as initial conditions and then carry out numerical simulations. Numerical solutions also allow the rotor acceleration phase to be included in simulations and consideration of concentration-dependent sedimentation/diffusion coefficients and chemical reactions among species.

The classical finite element method introduced in [3] uses a piecewise linear function to approximate the unknown concentration. It works very well for small- or medium-size molecules, providing approximations of high accuracy at moderate computational costs. But the method is troublesome for large molecules or high rotor speeds, when sedimentation is much stronger than diffusion, and is even unstable for the limiting case of no diffusion. Unappealing negative concentrations or large oscillations or both might also appear in the numerical solutions generated by the classical finite element method [4].

The moving hat method introduced in [4] is an improved finite element method based on a "moving" reference frame. The grid points are spaced exponentially to reflect the sedimentation speed. The two grid points at the meniscus and the cell bottom have to stay fixed physically. But the moving reference frame would require these two points to "move" like all other nodes in the grid. This singularity is remediated by manually adjusting the solution values at the node next to the meniscus and the node at the cell bottom. Another issue is that the grid spacing increases from the meniscus to the cell bottom, and hence results in lack of necessary spatial resolution near the cell bottom where the concentration gradients are large. This causes nonphysical oscillations in numerical solutions, especially when $\omega^2 s/D$ is large.

The space-time finite element method proposed in [5] overcomes this difficulty by introducing local spatial grid refinements near the cell bottom. But small time steps have to be used to obtain good numerical solutions. The method also assumes the same spatial partition for all time steps.

The complexity of numerically solving the Lamm equation is mainly due to the appearance of internal and boundary layers in the numerical solution. In this article, we develop a characteristic finite element method for the Lamm equation that overcomes the aforementioned difficulties and resolves the internal and boundary layers accurately and efficiently. First, we discuss some main features of the Lamm equation in section II. In section III, we present a full development of the characteristic finite element method, including discussions on local mesh refinements. In section IV, the characteristic method is validated through some numerical experiments. The article is concluded with some short remarks in section V.

II. SOME FEATURES OF THE SOLUTIONS OF THE LAMM EQUATION

Generally speaking, there is no analytical solution available for the Lamm equation, but some features of the solutions can be recognized and used to guide designing of efficient numerical methods.

A. Mass Conservation

The spatial variable r in the Lamm equation (1) appears in a one-dimensional fashion, but it is the radial position in the cylindrical coordinate system for the small centrifuge cell with a tiny angle θ. Recall that the area of a sector differential element is $(1/2)\theta d(r^2)$, and so the mass conservation for AUC takes the following form

$$\int_{r_{\mathrm{m}}}^{r_{\mathrm{b}}} c(r,t) r \, dr = \text{const}, \qquad \text{for any time } t, \tag{4}$$

instead of $\int_{r_{\mathrm{m}}}^{r_{\mathrm{b}}} c(r,t)\, dr = \text{const}$.

B. Characteristics

The velocity field in the ultracentrifuge cell is $\omega^2 sr$. Accordingly, a characteristic (streamline) passing through r^* at time t^* is defined as the solution of the following initial value problem of an ordinary differential equation (ODE)

$$\begin{cases} \dfrac{dr(t)}{dt} = \omega^2 sr, \\ r(t^*) = r^*, \end{cases} \tag{5}$$

which yields

$$r(t) = r^* \exp(\omega^2 s(t - t^*)). \tag{6}$$

One can then deduce that ideally

$$T = \frac{\ln(r_b/r_m)}{\omega^2 s}$$

is the time needed for a particle to travel from the meniscus to the cell bottom.

C. Moving and Broadening of Internal Layers

When diffusion is present ($D \neq 0$), the Lamm equation possesses some features of a parabolic equation. Starting with a uniform or differential initial concentration [2], an internal layer forms and moves toward the cell bottom. The width of the internal layer is proportional to $\sqrt{4Dt}$ [6] and the moving speed is $\omega^2 s$. This means that the numerical methods for the Lamm equation have to resolve the moving internal layers, especially in the early stage of a simulation process.

D. Radial Dilution

In the idealized case of no diffusion ($D = 0$) and an infinitely long cell ($r_b = \infty$), the Lamm equation is reduced to

$$\frac{\partial c}{\partial t} + \omega^2 sr \frac{\partial c}{\partial r} + 2\omega^2 sc = 0.$$

Since the total derivative along a characteristic is $\frac{dc}{dt} = \frac{\partial c}{\partial t} + \omega^2 sr \frac{\partial c}{\partial r}$, the Lamm equation is further reduced to the ODE $\frac{dc}{dt} = -2\omega^2 sc$, whose solution is

$$c(t) = c_0(r^*) e^{-2\omega^2 st},$$

where r^* is the starting point of a particle at time 0 that arrives at position r at time t. This indicates that the concentration is decreasing or being diluted at a rate of $e^{-2\omega^2 st}$.

E. The Steady-State

In the course of a sedimentation process, because of the strong centrifugal force, all particles will eventually sediment in a small region near the cell bottom, namely mass accumulates near the cell bottom. When the sedimentation process reaches its steady-state (equilibrium), one has $\partial c/\partial t = 0$.

Equivalently, the total flux vanishes everywhere, so a steady-state convection–diffusion type equation holds as follows

$$r D \frac{\partial c}{\partial r} - \omega^2 r^2 s c = 0, \qquad r \in [r_\mathrm{m}, r_\mathrm{b}]. \tag{7}$$

Solving the earlier equation yields $c_\infty(r) = K e^{\alpha r^2/2}$, where

$$\alpha = \frac{\omega^2 s}{D} \tag{8}$$

characterizes sedimentation-dominance of the solute transport and K is a constant to be determined from mass conservation. If the sedimentation process starts from a unity concentration profile, then

$$\frac{r_\mathrm{b}^2 - r_\mathrm{m}^2}{2} = \int_{r_\mathrm{m}}^{r_\mathrm{b}} r\, dr = K \int_{r_\mathrm{m}}^{r_\mathrm{b}} e^{\alpha r^2/2} r\, dr,$$

from which one solves for K and obtains the concentration distribution for the equilibrium:

$$c_\infty(r) = \frac{\alpha A}{1 - e^{-\alpha A}} e^{\alpha\left(r^2 - r_\mathrm{b}^2\right)/2}, \tag{9}$$

where for convenience we have defined the cross-section area

$$A = \frac{r_\mathrm{b}^2 - r_\mathrm{m}^2}{2}. \tag{10}$$

When α is large, i.e., the transport is sedimentation-dominated, we have

$$c_\infty(r_\mathrm{m}) \approx \alpha A\, e^{-\alpha A} \approx 0, \qquad c_\infty(r_\mathrm{b}) \approx \alpha A \gg 1.$$

Let r_a be such that $c_\infty(r_\mathrm{a}) = 1$, then $[r_\mathrm{a}, r_\mathrm{b}]$ is the region of *mass accumulation* and $[r_\mathrm{m}, r_\mathrm{a}]$ is the region of *mass depletion*, since $c_\infty(r)$ is strictly increasing. For convenience of calculations, we consider $r'_\mathrm{a} > r_\mathrm{a}$ with $c_\infty(r'_\mathrm{a}) = 1/(1 - e^{-\alpha A})$, which is equivalent to

$$\frac{r_\mathrm{b}^2 - \left(r'_\mathrm{a}\right)^2}{2} \Big/ \frac{r_\mathrm{b}^2 - r_\mathrm{m}^2}{2} = \frac{\ln(\alpha A)}{\alpha A} (\approx 0).$$

Applying the facts that $(1 - e^{-\alpha A}) \approx 1$ and $r'_\mathrm{a} \approx r_\mathrm{b}$, we obtain a good estimate

$$r_\mathrm{a} \approx r'_\mathrm{a} \approx r''_\mathrm{a} := r_\mathrm{b} - \frac{\ln(\alpha A)}{\alpha r_\mathrm{b}}. \tag{11}$$

For the steady-state, the concentration gradient is

$$c'_\infty(r) = \frac{\alpha A}{1 - e^{-\alpha A}} e^{\alpha\left(r^2 - r_\mathrm{b}^2\right)/2} \alpha r.$$

Clearly $c'_\infty(r)$ is also strictly increasing. Let r_s be such that $c'_\infty(r_s) = \beta$ and $[r_s, r_b]$ be defined as a steep region. Choosing $\beta = 1$ and mimicking the derivation of (11), we obtain

$$r_s \approx r_b - \frac{\ln((\alpha r_b)(\alpha A))}{\alpha r_b}. \tag{12}$$

The aforementioned discussions are for the ideal or steady-state cases, but the conclusions can be extended to the general case. In the sedimentation process of a homogeneous species with a uniform or differential initial concentration profile,

- An internal layer is moving at speed $\omega^2 s$ and broadening at a rate proportional to $\sqrt{4Dt}$;
- Before the internal layer reaches the cell bottom, a concentration plateau to the right of the internal layer can be observed and its height is decreasing at a rate of $e^{-2\omega^2 st}$;
- All particles eventually sediment in a region near the cell bottom, resulting in large concentration gradients in this small region. The width of the region is determined by the sedimentation-dominance parameter $\alpha = \omega^2 s/D$.

These features could be used to guide designing of efficient and robust numerical methods for the Lamm equation and local mesh refinements.

III. A CHARACTERISTIC FINITE ELEMENT METHOD WITH LOCAL MESH REFINEMENTS FOR THE LAMM EQUATION

A. Development of the Numerical Method

We rewrite the equation in an equivalent form as follows

$$r\frac{\partial c}{\partial t} + \frac{\partial}{\partial r}\left(\omega^2 r^2 sc - r\,D\frac{\partial c}{\partial r}\right) = 0, \qquad r \in [r_m, r_b], \quad t \in [t_0, t_f]. \tag{13}$$

It is also assumed that s and D are constants. The development of the numerical method is divided into two stages. A weak formulation based on a temporal discretization is first established. Then we apply a spatial finite element discretization to obtain a discrete algebraic system.

Let $t_0 < t_1 < \cdots < t_{n-1} < t_n < \cdots < t_N = t_f$ be a temporal partition of $[t_0, t_f]$ that is not necessarily uniform and $\Delta t_n = t_n - t_{n-1} (n = 1, \ldots, N)$. We consider test functions defined on the space-time slab $\Sigma = [r_m, r_b] \times [t_{n-1}, t_n]$. Multiplying both sides of Eq. (13) by a typical test function $\psi(r, t)$, we obtain

$$\int_{t_{n-1}}^{t_n}\int_{r_m}^{r_b}\left(r\frac{\partial c}{\partial t} + \frac{\partial}{\partial r}\left(\omega^2 r^2 sc - r\,D\frac{\partial c}{\partial r}\right)\right)\psi\; dr\, dt = 0. \tag{14}$$

For the first term in the earlier equation, Fubini's theorem and integration by parts in time yield

$$\int_{t_{n-1}}^{t_n}\int_{r_m}^{r_b} r\frac{\partial c}{\partial t}\psi\, dr\, dt = \int_{r_m}^{r_b}\left(\int_{t_{n-1}}^{t_n}\frac{\partial c}{\partial t}\psi\, dt\right) r\, dr = \int_{r_m}^{r_b} c(r, t_n)\psi(r, t_n) r\, dr$$
$$- \int_{r_m}^{r_b} c(r, t_{n-1})\psi\left(r, t_{n-1}^+\right) r\, dr - \int_{t_{n-1}}^{t_n}\int_{r_m}^{r_b} c\frac{\partial \psi}{\partial t} r\, dr\, dt. \tag{15}$$

For the second term in Eq. (14), we apply integration by parts in space and the no-flux boundary condition (3) to obtain

$$\int_{t_{n-1}}^{t_n}\int_{r_m}^{r_b}\frac{\partial}{\partial r}\left(\omega^2 r^2 sc - rD\frac{\partial c}{\partial r}\right)\psi\, dr\, dt = \int_{t_{n-1}}^{t_n}\left[\omega^2 r^2 sc - rD\frac{\partial c}{\partial r}\right]_{r_m}^{r_b}\psi\, dr\, dt - \int_{t_{n-1}}^{t_n}\int_{r_m}^{r_b}\left(\omega^2 r^2 sc - rD\frac{\partial c}{\partial r}\right)\frac{\partial \psi}{\partial r}dr\, dt. \quad (16)$$

A combination of the earlier two equations leads to

$$\int_{r_m}^{r_b} c(r,t_n)\psi(r,t_n)r\, dr + \int_{t_{n-1}}^{t_n}\int_{r_m}^{r_b} D\frac{\partial c}{\partial r}\frac{\partial \psi}{\partial r}r\, dr\, dt - \int_{t_{n-1}}^{t_n}\int_{r_m}^{r_b} c\left(\frac{\partial \psi}{\partial t} + \omega^2 sr\frac{\partial \psi}{\partial r}\right)r\, dr\, dt = \int_{r_m}^{r_b} c(r,t_{n-1})\psi\left(r,t_{n-1}^+\right)r\, dr. \quad (17)$$

We require each space-time test function to satisfy the adjoint equation

$$\frac{\partial \psi}{\partial t} + \omega^2 sr\frac{\partial \psi}{\partial r} = 0. \quad (18)$$

Clearly, this implies that any test function is a constant along each characteristic, i.e.,

$$\psi(r,t) = \psi(r^*,t^*). \quad (19)$$

We have now a weak formulation for the Lamm equation

$$\int_{r_m}^{r_b} c(r,t_n)\psi(r,t_n)r\, dr + \int_{t_{n-1}}^{t_n}\int_{r_m}^{r_b} D\frac{\partial c}{\partial r}\frac{\partial \psi}{\partial r}r\, dr\, dt = \int_{r_m}^{r_b} c(r,t_{n-1})\psi\left(r,t_{n-1}^+\right)r\, dr. \quad (20)$$

As shown in Fig. 2, the space-time slab $[r_m, r_b] \times [t_{n-1}, t_n]$is divided into three regions by two special characteristics: the one connecting$(r_m, t_{n-1})$and(r_m^+, t_n), and the one connecting (r_b^-, t_{n-1}) and (r_b, t_n), where

$$r_m^+ = r_m \exp(\omega^2 s\Delta t_n), \qquad r_b^- = r_b \exp(-\omega^2 s\Delta t_n). \quad (21)$$

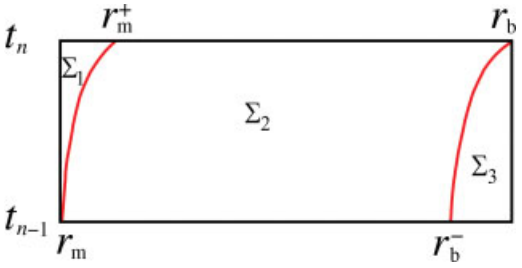

FIG. 2. The space-time slab $\Sigma = [r_m, r_b] \times [t_{n-1}, t_n]$ is divided into three regions $\Sigma_1, \Sigma_2, \Sigma_3$ by two special characteristics: the one connecting (r_m, t_{n-1}) and (r_m^+, t_n), and the one connecting (r_b^-, t_{n-1}) and (r_b, t_n). [Color figure can be viewed in the online issue, which is available at www.interscience.wiley.com.]

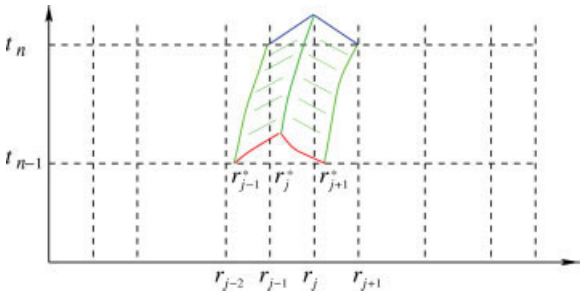

FIG. 3. An illustration of the test functions (except the last one). [Color figure can be viewed in the online issue, which is available at www.interscience.wiley.com.]

Next we consider spatial discretization and approximate the diffusion term in the weak form (20). For time step t_n, let $r_{\mathrm{m}} = r_0 < r_1 < \cdots < r_{j-1} < r_j < \cdots < r_M = r_{\mathrm{b}}$ with $h_j = r_j - r_{j-1} (j = 1, \ldots, M)$ be a nonuniform spatial mesh. We shall adopt local mesh refinements and Lagrangian $\mathcal{P}_1$ spatial elements at each time step. Let $\phi_j(r)$, $j = 0, \ldots, M$ be the nodal basis (hat) functions for a typical time step. Note that ϕ_0 has only the right half of the hat, whereas ϕ_M has only the left half. It should be pointed out that the spatial partition, the number of spatial elements M, and the nodal basis functions are generally different for different time steps. We shall assume this difference is clear from context rather than introduce some awkward notations.

Our finite element approximation is different than the traditional ones. The trial basis functions are spatial hat functions as described earlier, whereas the test basis functions are space-time functions that satisfy the adjoint Eq. (18). To be precise, let us look at a typical time stepping from t_{n-1} to t_n. The unknown approximate solution $C^{(n)}(r)$ at time step t_n is a linear combination of the spatial hat functions $\phi_j (j = 0, \ldots, M)$ with unknown coefficients $\{C_j^{(n)}\}_{j=0}^M$. There are $M + 1$ space-time test functions $\psi(r, t)$ that are defined in the space-time slab $\Sigma = [r_{\mathrm{m}}, r_{\mathrm{b}}] \times [t_{n-1}, t_n]$ and satisfy the adjoint equation. Any test function is a constant along each characteristic within its support. For $0 \le i \le (M - 1)$, $\psi_i(r, t_n) = \phi_i(r)$. So the support of $\psi_0(r, t)$is a region in Σ that is bounded by the boundary of Σ and the backtracking characteristic starting from(r_1, t_n). The support of $\psi_i(r, t)(i = 1, \ldots, M - 1)$ is a region in Σ that is bounded by the two backtracking characteristics starting from (r_{i-1}, t_n) and (r_{i+1}, t_n), respectively. An illustration of these test functions is shown in Fig. 3.

However, the last test function $\psi_M(r, t)$ is special. Its support consists of two parts. The first part is the region in Σ that is bounded by the two backtracking characteristics starting from

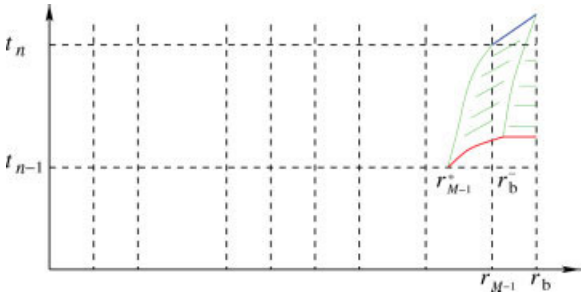

FIG. 4. An illustration of the last test function $\psi_M(r, t)$. [Color figure can be viewed in the online issue, which is available at www.interscience.wiley.com.]

(r_{M-1}, t_n) and (r_M, t_n), respectively. Similarly, $\psi_M(r, t_n) = \phi_M(r)$. The second part of the support is Σ_3 and $\psi_M(r, t) \equiv 1$ on Σ_3, see Fig. 4. The last test function is so specially constructed because of the physical properties of the sedimentation process. The solute flows outward in the radial position. The solute mass distributed in the region $[r_{\mathrm{b}}^-, r_{\mathrm{b}}]$ at time t_{n-1} will reach the cell bottom r_{b} during the time period $[t_{n-1}, t_n]$. In other words, we take into account the mass accumulation at cell bottom r_{b} during the time period $[t_{n-1}, t_n]$.

For the diffusion term in the weak form (20), our treatment is similar to that in [7]. Because the diffusion is small, the test functions are constants along characteristics, and the solution changes the least along characteristics, and we approximate the diffusion term as

$$\int_{t_{n-1}}^{t_n} \int_{r_{\mathrm{m}}}^{r_{\mathrm{b}}} D \frac{\partial c}{\partial r} \frac{\partial \psi}{\partial r} r \, dr \, dt \approx \int_{r_{\mathrm{m}}}^{r_{\mathrm{b}}} \Delta t(r, t_n) D \frac{\partial C^{(n)}(r)}{\partial r} \frac{\partial \psi}{\partial r}(r, t_n) r \, dr, \tag{22}$$

where $\Delta t(r, t_n) = t_n - t^*$ and (r^*, t^*) is the foot of the characteristic starting from (r, t_n). This approximation holds for all test basis functions. Clearly, if $r_{\mathrm{m}} \le r < r_{\mathrm{m}}^+$, then $t^* \in (t_{n-1}, t_n]$ and hence $\Delta t(r, t_n) < \Delta t_n$. But if $r_{\mathrm{m}}^+ \le r \le r_{\mathrm{b}}$, then $t^* = t_{n-1}$ and hence $\Delta t(r, t_n) = \Delta t_n$.

Substituting (20) into (22), we obtain a finite element scheme for the Lamm equation. At each time step $t_n (1 \le n \le N)$, seek

$$C^{(n)}(r) = \sum_{j=0}^{M} C_j^{(n)} \phi_j(r) \tag{23}$$

such that for any test function $\psi(r, t)$, the following holds

$$\int_{r_{\mathrm{m}}}^{r_{\mathrm{b}}} C^{(n)}(r) \psi(r, t_n) r \, dr + \int_{r_{\mathrm{m}}}^{r_{\mathrm{b}}} \Delta t(r, t_n) D \frac{\partial C^{(n)}(r)}{\partial r} \frac{\partial \psi}{\partial r}(r, t_n) r \, dr = \int_{r_{\mathrm{m}}}^{r_{\mathrm{b}}} C^{(n-1)}(r) \psi\left(r, t_{n-1}^+\right) r \, dr. \tag{24}$$

To start the time-stepping procedure, $C^{(0)}(r)$ can be taken as the piecewise linear nodal interpolation of the initial condition $c_0(r)$.

Next we discuss how to evaluate the mass matrix, the stiffness matrix, and the right-hand side in the discrete linear system. The mass matrix

$$\mathbf{A} = [A_{i,j}]_{(M+1)\times(M+1)} = \left[\int_{r_{\mathrm{m}}}^{r_{\mathrm{b}}} \phi_i(r) \phi_j(r) r \, dr \right]_{i,j=0,\ldots,M} \tag{25}$$

is a symmetric tridiagonal matrix. In particular, we have

$$\begin{aligned} A_{0,0} &= \frac{1}{12}(r_1 - r_0)(r_1 + 3r_0), \qquad A_{0,1} = \frac{1}{12}\left(r_1^2 - r_0^2\right), \\ A_{i,i-1} &= \frac{1}{12}\left(r_i^2 - r_{i-1}^2\right), \qquad A_{i,i+1} = \frac{1}{12}\left(r_{i+1}^2 - r_i^2\right), \\ A_{i,i} &= \frac{1}{12}(r_i - r_{i-1})(3r_i + r_{i-1}) + \frac{1}{12}(r_{i+1} - r_i)(r_{i+1} + 3r_i), \\ A_{M,M-1} &= \frac{1}{12}\left(r_M^2 - r_{M-1}^2\right), \qquad A_{M,M} = \frac{1}{12}(r_M - r_{M-1})(3r_M + r_{M-1}), \end{aligned} \tag{26}$$

where $1 \le i \le (M-1)$.

The stiffness matrix

$$\mathbf{B} = [B_{i,j}]_{(M+1)\times(M+1)} = \left[\int_{r_\mathrm{m}}^{r_\mathrm{b}} \Delta t_n(r,t_n) D \frac{\partial \phi_i}{\partial r}\frac{\partial \phi_j}{\partial r} r\, dr\right]_{i,j=0,\ldots,M} \tag{27}$$

is also a symmetric tridiagonal matrix, but its evaluation is a little bit more involved, since $\Delta t_n(r,t_n)$ relies on characteristic tracking. Suppose $r_\mathrm{m}^+ \in (r_{I-1}, r_I]$ for some $I \geq 1$ (but $I \ll M$). It is known that $\Delta t(r,t_n) = \Delta t_n$ for $r \geq r_\mathrm{m}^+$. So explicit expressions are available for the following entries:

$$B_{i,i-1} = -\Delta t_n D \frac{1}{2}\frac{r_i + r_{i-1}}{r_i - r_{i-1}}, \qquad B_{i,i+1} = -\Delta t_n D \frac{1}{2}\frac{r_{i+1} + r_i}{r_{i+1} - r_i},$$

$$B_{i,i} = \Delta t_n D \frac{1}{2}\left(\frac{r_i + r_{i-1}}{r_i - r_{i-1}} + \frac{r_{i+1} + r_i}{r_{i+1} - r_i}\right), \qquad \text{for } (I+1) \leq i \leq (M-1),$$

$$-B_{M,M-1} = B_{M,M} = \Delta t_n D \frac{1}{2}\frac{r_M + r_{M-1}}{r_M - r_{M-1}}. \tag{28}$$

For the evaluation of $B_{0,0}, B_{0,1} = B_{1,0}, B_{1,1}, B_{1,2}$ until $B_{I,I-1}, B_{I,I}$, Gaussian quadratures could be employed.

The evaluation of the right-hand side of (24) depends on the test functions and characteristic tracking. For the first few test basis functions, their supports do not intersect with $[r_\mathrm{m}, r_\mathrm{b}] \times \{t_{n-1}\}$, so $\psi(r, t_{n-1}^+) = 0$ and hence the corresponding entries are zero. For a test function whose support intersects with $[r_\mathrm{m}, r_\mathrm{b}] \times \{t_{n-1}\}$, we apply change of variable to evaluate the integral. For simplicity of presentation, we assume that both supp $\psi(r,t_n)$ and supp $\psi(r,t_{n-1}^+)$ are in $[r_\mathrm{m}, r_\mathrm{b}]$. We replace the dummy integral variable r by r^* and rewrite the integral as

$$\int_{r_\mathrm{m}}^{r_\mathrm{b}} C^{(n-1)}(r^*)\psi\left(r^*, t_{n-1}^+\right) r^* dr^*.$$

Note that (6) defines a one-to-one mapping between supp $\psi(r,t_n)$ and supp $\psi(r,t_{n-1}^+)$, so we have

$$\int_{r_\mathrm{m}}^{r_\mathrm{b}} C^{(n-1)}(r^*)\psi\left(r^*, t_{n-1}^+\right) r^*\, dr^* = e^{-2\omega^2 s \Delta t_n} \int_{r_\mathrm{m}}^{r_\mathrm{b}} C^{(n-1)}(r^*)\psi(r,t_n) r\, dr.$$

The earlier right-hand side could be evaluated by a Gaussian quadrature on supp $\psi(r,t_n)$, therein $C^{(n-1)}(r^*)$ is evaluated through linear interpolation after r^* is located.

Once again the evaluation of the right-hand side involving the last test basis function $\psi_M(r,t)$ is divided into two parts because of the two-part structure of its support. The calculation on the left part is similar to what is just described earlier. The right part is simply

$$\int_{r_\mathrm{b}^-}^{r_\mathrm{b}} C^{(n-1)}(r) r\, dr,$$

because $\psi_M(r,t) \equiv 1$ on Σ_3. An explicit formula is available for the earlier integral, since $C^{(n-1)}(r)$ is piecewise linear on $[r_\mathrm{b}^-, r_\mathrm{b}]$.

Finally, we obtain a tridiagonal linear system with unknowns $\{C_j^{(n)}\}_{j=0}^M$ and the coefficient matrix $(\mathbf{A} + \mathbf{B})$. The linear system can be solved directly with spatial and temporal complexities both $\mathcal{O}(M)$.

B. Local Mesh Refinements

As discussed in section II, in the course of a sedimentation process, mass builds up in a small region near the cell bottom. Resolving the large concentration gradients in this region requires a high spatial resolution. It has been pointed out in [4] that lack of sufficient spatial resolution near the cell bottom results in nonphysical oscillations in numerical solutions. Internal layers (simply called boundaries in AUC) also appear in sedimentation experiments. Between the internal and boundary layers, concentration plateaus are observed as well. A very fine uniform mesh will unnecessarily increase computational cost. This calls for a spatial mesh with local mesh refinements that reflect the spatial features of the solution. This could be a well-designed static mesh that works for the entire course of a sedimentation process, or a dynamic mesh that changes in time steps.

Our characteristic method provides a flexible framework in this regard. Different optimal spatial meshes can be used for different time steps, or a static spatial mesh with well-designed local refinements could be adopted for the entire sedimentation course. In this subsection, we investigate local refinements near the cell bottom and the moving internal layer.

It can be shown that the boundary condition (3) implies some restrictions on the spatial mesh. The approximate solution is a piecewise linear polynomial and hence

$$\left.\frac{\partial C}{\partial r}\right|_{r=r_{\mathrm{b}}} = \left.\frac{\partial C}{\partial r}\right|_{r=r_M} = \frac{C_M - C_{M-1}}{r_M - r_{M-1}}.$$

The second condition in (3) is then translated into

$$-C_{M-1} + \left[1 - \frac{\omega^2 s}{D} r_M (r_M - r_{M-1})\right] C_M = 0, \tag{29}$$

which implies that one must have

$$(r_M - r_{M-1}) < \frac{1}{\alpha r_{\mathrm{b}}}, \tag{30}$$

to avoid oscillations in the numerical solution at the cell bottom. A similar condition can be derived from the general discussion in [8] on why large local Peclet numbers are needed in steep regions for convection-dominated fluid transport problems.

Based on the discussions in section II, we choose

$$r_{\mathrm{s}} = r_{\mathrm{b}} - \frac{\ln((\alpha r_{\mathrm{b}})(\alpha A))}{\alpha r_{\mathrm{b}}} \tag{31}$$

and arrange grid points in the steep region $[r_{\mathrm{s}}, r_{\mathrm{b}}]$. These grid points could be uniformly distributed on $[r_{\mathrm{s}}, r_{\mathrm{b}}]$ or in a sine-distribution as described in [5]. To be precise, we define

$$h_s = \frac{1}{\alpha r_{\mathrm{b}}}, \qquad M_s = \mathrm{ceil}\left(\frac{\pi}{2}\frac{r_{\mathrm{b}} - r_{\mathrm{s}}}{h_{\mathrm{s}}}\right), \tag{32}$$

where $\mathrm{ceil}(z)$ is the smallest integer that is no smaller than z. Then we define

$$z_k = r_{\mathrm{s}} + (r_{\mathrm{b}} - r_{\mathrm{s}}) \sin\left(\frac{k}{M_{\mathrm{s}}}\frac{\pi}{2}\right), \qquad k = 0, 1, \ldots, M_{\mathrm{s}}. \tag{33}$$

It can be verified that

$$z_k - z_{k-1} \approx h_s \cos\left(\frac{k-1}{M_s}\frac{\pi}{2}\right), \qquad k = 1, \ldots, M_s.$$

In particular,

$$z_M - z_{M-1} \approx \frac{\pi}{2M_s} h_s.$$

Given a quasi-uniform temporal partition $t_0 < t_1 < \cdots < t_{n-1} < t_n < \cdots < t_N = t_f \leq T = \ln(r_b/r_m)/(\omega^2 s)$, we know that, for time t_n, the internal layer is centered at radial position $r_m e^{\omega^2 s(t_n - t_0)}$. We could set grid points to "catch" these steep fronts. To be precise, we choose $M_r < N$ and set

$$r_0 = r_m, \quad r_1 = r_m e^{\omega^2 s(t_1 - t_0)/2}, \quad r_j = r_m e^{\omega^2 s((t_{j-1}+t_j)/2 - t_0)}, \quad j = 2, \ldots, M_r. \tag{34}$$

In the case of a uniform temporal partition, this is similar to the grid distribution in the moving hat method [4]. In practice, one can choose $M_r = N - 2$ or $N - 1$, so that r_{M_r} is very close to r_b. Let $r_t = r_{M_r}$, then $[r_m, r_t]$ is called the regular region.

As usual in most other cases of local mesh refinements, a transitional region is needed between the regular and steep regions. Several transitional elements are placed in the transitional region $[r_t, r_s]$. Each has a half length of its left neighbor. The leftmost element has a size about $r_{M_r} - r_{M_{r-1}}$ whereas the rightmost has a size about h_s.

Another eminent feature of the solution of the Lamm equation is the sharp internal layer in the early stage of the sedimentation course. Let $\delta t = t_1 - t_0$. Because of the parabolic feature of the Lamm equation, the internal layer width is about $\sqrt{4D\delta t}$ at time t_1. If the Schuck's "moving" grid is used, then the second element has width $r_2 - r_1 \approx r_m \omega^2 s\ \delta t$. To avoid oscillations in the numerical solution near the meniscus, one should have

$$r_m \omega^2 s\ \delta t \leq \sqrt{4D\,\delta t}, \tag{35}$$

so that the element indeed "catches" the sharp internal layer. If N is the number of time steps, then a direct calculation yields

$$N \geq \frac{1}{4}\alpha r_m^2 \ln\left(\frac{r_b}{r_m}\right), \tag{36}$$

which implies a high spatial resolution near the meniscus is also needed when α is large. For the space-time finite element method in [5], this means both numbers of time steps and spatial grid points are increased, But for the characteristic finite element method discussed in this article, we could just refine the spatial mesh locally near the meniscus (increase the CFL number), without unnecessarily increasing the number of time steps. The grid points around the internal layers could be in a sine-distribution or a doubling-distribution.

C. Features of the Numerical Method

In this subsection, we outline the main features of the characteristic finite element method for the Lamm equation.

Mass Conservation. By construction, $\sum_{i=0}^{M} \psi_i(r,t) \equiv 1$ on the space-time slab $[r_m, r_b] \times [t_{n-1}, t_n]$. Combined with (24), this implies that

$$\int_{r_m}^{r_b} C^{(n)}(r) r \, dr = \int_{r_m}^{r_b} C^{(n-1)}(r) r \, dr. \tag{37}$$

Therefore, our numerical scheme is mass-conservative by design. Since piecewise linear approximations to the unknown concentration are adopted in our numerical scheme, an explicit formula for computing the total mass at a typical time step t_n is available as follows

$$\int_{r_m}^{r_b} C^{(n)}(r) r \, dr = \sum_{j=1}^{M} \left[\frac{1}{2}(r_{j-1} + r_j)\left(r_j C_{j-1}^{(n)} - r_{j-1} C_j^{(n)}\right) + \frac{1}{3}\left(r_{j-1}^2 + r_{j-1} r_j + r_j^2\right)\left(C_j^{(n)} - C_{j-1}^{(n)}\right) \right]. \tag{38}$$

However, the evaluations of the coefficient matrix entries and the right-hand side of the linear system involve quadrature errors and round-off errors, the actual total mass might fluctuate slightly from time to time. The aforemention formula can be used for checking mass conservation in numerical experiments.

CFL-Free. First, the method developed in this article is not subject to the severe restrictions of the Courant-Friedrichs-Lewy (CFL) condition. Our numerical scheme is unconditionally stable, and so relatively large time steps can be used in numerical simulations and hence computational cost is reduced. While in the traditional finite element method [3], small time steps have to be used because of the restrictions of the CFL condition.

Varying Spatial Meshes. In our numerical method, different spatial partitions can be used at different time steps to accommodate the moving internal layers or other spatial features in the solutions. For the adaptive space-time finite element method (ASTFEM) in [5], it could be very difficult to connect spatial nodes at two adjacent time steps to form space-time finite elements if the two spatial partitions are different. In this situation, it is also unclear how the test functions in ASTFEM should be defined.

Efficient Characteristic Tracking. Characteristic tracking is an important part of our numerical scheme. Actually, we have an explicit formula (6) for tracking. The real cost is on locating the foot or head of a characteristic in an unstructured mesh (at time step t_{n-1}). Similar to the techniques proposed in [9], an auxiliary one-dimensional uniform mesh and then a look-up table can be established and utilized to facilitate the locating process. Or the known structure of a spatial mesh can be exploited for the locating task. For example, for a spatial mesh with local refinements discussed in this paper and [5], a point of interest can be first located in a regular region, a transitional region, or a steep region. Then the mesh structure of the region can be used to further locate the very element containing the point.

Positivity and Monotonicity of Numerical Solutions. With the local mesh refinements in the steep regions near the cell bottom and/or around the internal layer, the numerical solutions

generated by our numerical scheme are free of nonphysical oscillations. Positivity and monotonicity are well kept in numerical solutions. In particular, the following formula for the total variation of the numerical solution at a typical time step t_n

$$\mathrm{TV}[C^{(n)}(r)] = \sum_{j=1}^{M} \left| C^{(n)}(r_j) - C^{(n)}(r_{j-1}) \right| \tag{39}$$

can be used for monitoring oscillations.

Radial Dilution. This property is also clearly reflected in our characteristic method. From Eq. (6), we have

$$r^* = r\exp(-\omega^2 s(t-t^*)), \qquad dr^* = dr\exp(-\omega^2 s(t-t^*)).$$

Replacing the dummy integral variable r on the right-hand side of (24) by r^*, and then combining the earlier two formulas with Eqs. (19) and (24), we obtain

$$\begin{aligned}\int_{r_\mathrm{m}}^{r_\mathrm{b}} c(r,t_n)\psi(r,t_n) r\,dr &= \int_{r_\mathrm{m}}^{r_\mathrm{b}} c(r^*,t_{n-1})\psi\left(r^*,t_{n-1}^+\right) r^*\,dr^* \\ &= \int_{r_\mathrm{m}}^{r_\mathrm{b}} c(r^*,t_{n-1})\psi(r,t_n)\exp(-2\omega^2 s(t_n-t_{n-1})) r\,dr.\end{aligned}$$

But $\psi(r,t_n)$ is arbitrary, so we have

$$c(r,t_n) = c(r^*,t_{n-1})\, e^{-2\omega^2 s(t_n - t_{n-1})}, \tag{40}$$

which is the radial dilution property, as anticipated.

IV. NUMERICAL EXPERIMENTS

In this section, we test our numerical method on two examples to demonstrate its efficiency and robustness. In the first example, we compare our numerical results with the raw data from an AUC experiment. In the second example, we compare our method with the space-time finite element method in [5]. In AUC, the sedimentation coefficients are measured in Svedberg (S) and 1S = 10^{-13} s, the unit for diffusion coefficients is cm^2/s. But the angular velocity ω is usually expressed as rpm (revolutions per minute), so we need the conversion $\omega/60 \times (2\pi) = \omega \times \pi/30$ (radian per second).

Example 1. We obtained some raw data on a relatively homogeneous sample from an AUC experiment in a Beckman Optima XL-I AUC with the absorbance detection system. The raw data were processed by the UltraScan software [10]. The van-Holde-Weischet method [11] was used to derive the sedimentation coefficient $s = 2.9077 \times 10^{-13}$. Assume the molecules are prolate ellipsoids, the diffusion coefficient is fitted as $D = 5.0383 \times 10^{-7}$. The angular velocity is $\omega = 50{,}000(\mathrm{rpm}) \approx 5236(\mathrm{radian/second})$. So $\alpha = \omega^2 s/D \approx 15.8$. The estimated meniscus is $r_\mathrm{m} = 6.123(\mathrm{cm})$ and the cell bottom is $r_\mathrm{b} = 7.2(\mathrm{cm})$. So $T = \ln(r_\mathrm{b}/r_\mathrm{m})/(\omega^2 s) = 20325(\mathrm{seconds}) \approx 339(\mathrm{minutes}) \approx 5°38'45''$. The loading concentration (initial condition) is 0.527061(OD). A sequence of 60 scans were attempted during the course of about 195 min, but

TABLE I. Example 1: Fitted and simulated plateau concentrations (OD) versus corrected time (min′sec″).

Time	Fitted	Simulated
004′00″	0.526	0.525
007′57″	0.524	0.523
011′34″	0.522	0.521
014′55″	0.520	0.519
018′00″	0.519	0.518
021′08″	0.517	0.516
024′11″	0.515	0.515
027′15″	0.514	0.513
030′31″	0.512	0.511
033′35″	0.510	0.510
036′35″	0.509	0.508
039′45″	0.507	0.507
042′53″	0.505	0.505
046′00″	0.504	0.504
049′06″	0.502	0.502
052′05″	0.501	0.501
055′08″	0.499	0.499
058′16″	0.498	0.498
061′21″	0.496	0.497
064′24″	0.494	0.495
067′27″	0.493	0.494
070′32″	0.491	0.492
073′58″	0.490	0.491
078′28″	N/A	0.489
083′08″	0.485	0.486
086′15″	0.483	0.485
089′18″	0.482	0.483
092′25″	0.480	0.482
095′48″	0.479	0.480
098′54″	0.477	0.479
102′06″	0.476	0.478
105′13″	0.474	0.476
108′20″	0.473	0.475
111′24″	0.471	0.473
114′42″	0.469	0.472
117′54″	0.468	0.470
121′00″	0.466	0.469
124′08″	0.465	0.468
127′23″	0.463	0.466
130′49″	0.462	0.465
133′58″	0.460	0.463
137′09″	0.459	0.462
140′16″	0.457	0.460
143′16″	0.456	0.459
146′18″	0.454	0.458
149′27″	0.453	0.456
152′46″	0.451	0.455
155′49″	0.450	0.454
158′54″	0.449	0.452
162′09″	0.447	0.451
165′14″	0.446	0.449
168′18″	0.444	0.448
171′30″	0.443	0.447
174′31″	0.441	0.445
177′37″	0.440	0.444
180′38″	0.439	0.442
183′47″	0.437	0.440
187′02″	0.436	0.438
190′10″	0.434	0.436
193′19″	0.433	0.434

the 24th scan was missed in the operation. Accordingly, the initial and final simulation times are respectively $t_0 = 0$ and $t_f = 195$(min). Because of the equipment limitation, the data acquired near the meniscus and the cell bottom are not really meaningful. For this particular case, the window for data fitting is chosen as $[6.20, 7.10]$.

For this example, the 60 time moments when the AUC equipment recorded the concentration data are shown in Table I. These also form the temporal partition used in our numerical simulation, which means a relative large time step about 4 min. The steep region is set as $[7.1168, 7.2]$ that contains 15 elements. Only 118 elements are used in the whole region, but our numerical results are still fairly accurate. The numerical solutions are monotone and positive for all 60 time moments. There is not any oscillation in the numerical solutions near the cell bottom or the meniscus. Since an initial uniform loading concentration 0.527061 is used, the total mass is 3.78137. For the 60 time moments in the numerical simulation, the total mass varies in the interval $[3.78020, 3.78147]$. This means the error in the total mass is only about 0.03%. The fitted concentration plateaus in the experiment data and the calculated concentration plateaus in the numerical solutions are shown in Table I. The discrepancies are within 1%. Shown in Fig. 5 are the concentration distribution curves from the experiment data and the numerical simulations. The wiggles in the experimental concentration distribution curves are due to the equipment noises. Shown in Fig. 6 are respectively the experiment and numerical concentration curves for the 25th scan (time $t = 83'08''$) and the 50th scan ($t = 162'09''$).

Example 2. In this example studied in [5], $r_m = 5.8, r_b = 7.2, \omega = 50{,}000$(rpm), $s = 1.562 \times 10^{-12}$, $D = 1.279 \times 10^{-7}$. So $\alpha \approx 334.8$ and $T \approx 5050$(s) $= 1°24'10''$.

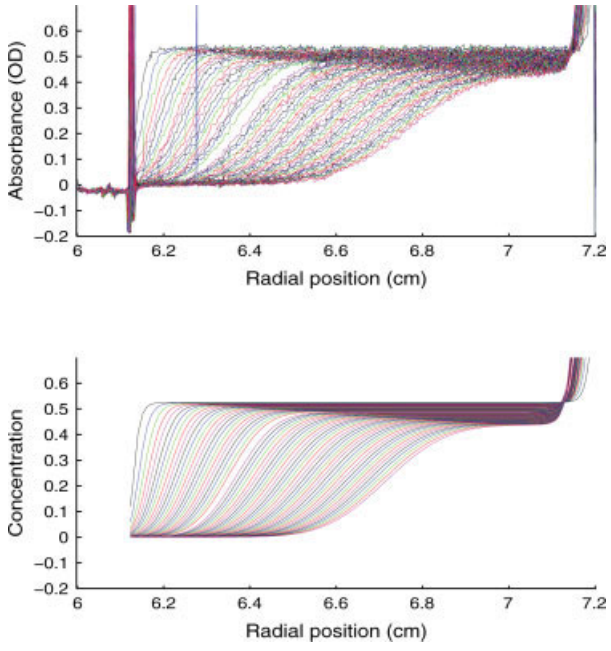

FIG. 5. Example 1: All concentration distribution curves: Upper plot: experimental scans; Lower plot: numerical simulations. [Color figure can be viewed in the online issue, which is available at www.interscience.wiley.com.]

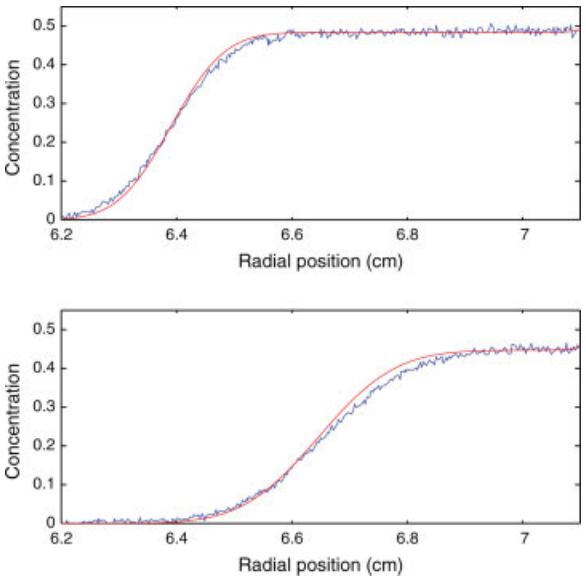

FIG. 6. Example 1: Experimental and numerical concentration distributions on [6.2, 7.1]: Upper plot: the 25th scan $t = 83'08''$; Lower plot: the 50th scan $t = 162'09''$. [Color figure can be viewed in the online issue, which is available at www.interscience.wiley.com.]

This example was also studied in [5]. Even though the large concentration gradients near the cell bottom are well resolved, negative concentrations near the meniscus in the numerical solution can still be observed unless N is large, see Fig. 9 in [5]. When $N = 100$, the negative concentrations are at the magnitude 10^{-3}. For $N = 200$, the magnitude is 10^{-4}; for $N = 400$, magnitude 10^{-7}. Negative concentrations near the meniscus remain until $N > 820$. This phenomenon is well explained by Formula (36) in this paper.

TABLE II. Example 2: Info on the dynamic meshes used in the characteristic finite element method.

	Number of elements				
Time (s)	Before the front	Around the front	Plateau region	Near cell bottom	Total
0	N/A	N/A	N/A	N/A	280
101	20	30	229	25	304
404	49	28	213	25	315
1010	83	26	186	25	320
2525	140	27	116	25	308

TABLE III. Example 2: Numerical solutions of the characteristic FEM.

Time (s)	Total mass	Min (at r_m)	Max (at r_b)	Total variation	Concentration plateau
0	9.1	1	1	0	1
101	9.0997	3.928 E−6	13.184	13.184	0.991
404	9.0997	8.538 E−15	49.111	49.111	0.965
1010	9.0997	1.319 E−31	118.227	118.227	0.917
2525	9.0997	4.568 E−77	276.107	276.107	0.805

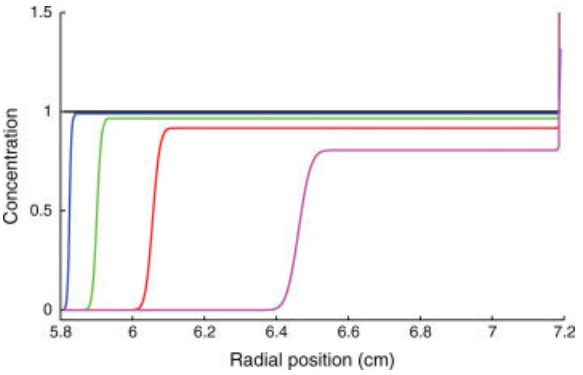

FIG. 7. Example 2: Numerical solutions on [5.814, 7.186] at $t = 101, 404, 1010, 2525$ (s). [Color figure can be viewed in the online issue, which is available at www.interscience.wiley.com.]

For the characteristic FEM with local mesh refinements, larger time steps and fewer finite elements are used. In our numerical experiments, we use $N = 100$ and hence $\Delta t = 50.5$(s). We apply local mesh refinements, both around the moving internal layer and near the cell bottom. Tables II and III list some statistics for the meshes and the numerical solutions at different time moments. Figure 7 shows the graphs of the numerical solutions in [5.814, 7.186] at $t = 101, 404, 1010, 2525$ (s). It can be observed that the positivity and monotonicity of the numerical solution are well kept.

V. CONCLUDING REMARKS

Solving the Lamm equation accurately and efficiently is an important aspect in AUC, for example, the size distribution analysis discussed in [12]. In this article, we have developed an efficient numerical method for the linear Lamm equation. When the sedimentation and diffusion coefficients depend on the unknown concentration, the Lamm equation becomes nonlinear and hence more difficult to solve. A mass-conservative finite volume method for the nonlinear Lamm equation is under our investigation.

The authors express their sincere thanks to Drs. Weiming Cao, Borries Demeler, Steve McBryant, and Simon Tavener for the interesting discussions and their kind help. We also thank the anonymous reviewers, whose comments have helped improve the quality of this paper.

References

1. T. M. Laue and W. F. Stafford III, Modern applications of analytical ultracentrifugation, Annu Rev Biophys Biomol Struct 28 (1999), 75–100.
2. H. Fujita, Foundations of ultracentrifugal analysis, Wiley, New York, 1975.
3. J. M. Claverie, H. Dreux, and R. Cohen, Sedimentation of generalized systems of interacting particles. I. Solutions of systems of complete Lamm equations, Biopolymers 14 (1975), 1685–1700.
4. P. Schuck, Sedimentation analysis of noninteracting and self-associating solutes using numerical solutions to the Lamm equation, Biophys J 75 (1998), 1503–1512.
5. W. Cao and B. Demeler, Modeling analytical ultracentrifugation experiments with an adaptive space-time finite element solution of the Lamm equation, Biophys J 89 (2005), 1589–1602.

6. L. C. Evans, Partial differential equations, American Mathematical Society, Providence, RI, 1998.
7. H. Wang, H. K. Dahle, R. E. Ewing, M. S. Espedal, R. C. Sharpley, and S. Man, An ELLAM scheme for advection-diffusion equations in two dimensions, SIAM J Sci Comput 20 (1999), 2160–2194.
8. K. W. Morton, Numerical solutions of convection–diffusion problems, Chapman & Hall, London, 1996.
9. J. Liu, H. Chen, R. E. Ewing, and G. Qin, An efficient algorithm for characteristic tracking on two-dimensional triangular meshes, Computing 80 (2007), 121–136.
10. B. Demeler, The UltraScan software package—a comprehensive data analysis package for sedimentation experiments, Available at http://www.ultrascan.uthscsa.edu/.
11. K. E. van Holde and W. O. Weischet, Boundary analysis of sedimentation velocity experiments with monodisperse and paucidisperse solutes, Biopolymers 17 (1978), 1387–1403.
12. P. Schuck, Size distribution analysis of macromolecules by sedimentation velocity ultracentrifugation and Lamm equation modeling, Biophys J 78 (2000), 1606–1619.